Energy 338 (2025) 138527

Contents lists available at ScienceDirect

Energy

journal homepage: www.elsevier.com/locate/energy

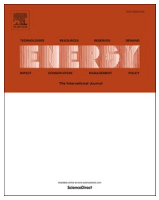

Exploring waste heat recovery from applied smouldering systems

Ryan B. Morales [a,b], Tarek L. Rashwan [c,d,e,*], Marco A.B. Zanoni [a], Christopher T. DeGroot [f], Jason I. Gerhard [a,1]

[a] Department of Civil and Environmental Engineering, The University of Western Ontario, London, N6A 3K7, Canada
[b] Savron Solutions, Cambridge, N3E 1A5, Canada
[c] Department of Civil Engineering, Lassonde School of Engineering, York University, Toronto, M3J 1P3, Canada
[d] School of Engineering & Innovation, The Open University, Milton Keynes, MK7 6AA, United Kingdom
[e] Food Water Waste Research Group, Faculty of Engineering, University of Nottingham, University Park, Nottingham, NG7 2RD, UK
[f] Department of Mechanical and Materials Engineering, The University of Western Ontario, Canada

ARTICLE INFO

Keywords:
Applied smouldering
Numerical model
Energy efficiency
Waste heat recovery
Thermal treatment
Waste-to-energy

ABSTRACT

Applied smouldering systems are used to treat stockpiles of contaminated soils as well as organic liquid/sludge wastes intentionally mixed within a porous medium (e.g., sand). These systems treat virtually all contaminants/wastes, and leave behind a hot, clean, porous media. Large amounts of excess thermal energy are generated during smouldering and ultimately exhausted to the external environment when the hot bed is convectively cooled after treatment. This wasted heat can be harnessed to offset system energy requirements and enhance this system's sustainability, reduce environmental impact, and improve economic competitiveness. In this study, a novel three-dimensional numerical model was developed to simulate treatment bed cooling after smouldering and explore the waste heat recovery potential. Key system parameters and bed temperature data from a real-world commercial smouldering application were used to construct the model boundary and initial conditions. This model quantified the temporal availability and quality (i.e., exergy) of the exhaust waste heat for the first time. The model showed how the practical cooling period lasted 4.1 days, where 86 % of the energy stored in the bed was exhausted over this time and the energy release rate was governed by the bed's cooling velocity. Moreover, it was found that the cumulative output exergy during the cooling phase was 45 % of the cumulative electrical energy needed to drive equipment during the smouldering phase. Therefore, this waste heat could substantially offset the energy requirements in neighbouring systems. Overall, this study reveals the significant opportunity for waste heat recovery from applied smouldering systems.

Nomenclature

Abbreviations	
LTNE	Local Thermal Non-Equilibrium
PFAS	Per- and polyfluoroalkyl substances
WHR	Waste Heat Recovery
STARx	Self-sustaining Treatment for Active Remediation ex situ
TC	Thermocouple
Latin Letters	
A_i	Cell surface area, m^2
A_{sg}	Specific surface area, m^{-1}
C_p	Specific heat capacity, J kg^{-1} K^{-1}
d_p	Particle diameter, m
e	Specific energy, J kg^{-1}

(*continued on next column*)

(*continued*)

E	Energy, J
$\dot{E}$	Energy rate, J s^{-1}
g	Gravity acceleration, m s^{-2}
h_{sg}	Interfacial heat transfer coefficient, W m^{-2} K^{-1}
k	Thermal conductivity, W m^{-1} K^{-1}
k_{int}	Intrinsic permeability, m^2
M_w	Molecular weight of air, kg mol^{-1}
n	Total number of cells in calculation
Nu	Nusselt number
Pr	Prantl number
P	Pressure, Pa
q_g	Darcy flux, m s^{-1}
R	Ideal gas coefficient, J mol^{-1} K^{-1}

(*continued on next page*)

* Corresponding author. Food Water Waste Research Group, Faculty of Engineering, University of Nottingham, University Park, Nottingham, NG7 2RD, UK.
E-mail address: tarek.rashwan@nottingham.ac.uk (T.L. Rashwan).
[1] Deceased.

https://doi.org/10.1016/j.energy.2025.138527
Received 16 July 2025; Received in revised form 28 August 2025; Accepted 15 September 2025
Available online 6 October 2025

(*continued*)

Re	Reynolds number
t	Time, s
T	Temperature, K
$\overline{T}$	Mass averaged temperature, K
v_{cool}	Cooling velocity, m s^{-1}
V_i	Cell volume
Greek Symbols	
ϕ	Porosity
ρ	Density, kg m^{-3}
μ_g	Gas dynamic viscosity, Pa S
σ	Stefan-Boltzmann constant, W m^{-2} K^{-4}
Ξ	Exergy, J
$\dot{\Xi}$	Exergy rate, J s^{-1}
Subscripts	
amb	Ambient
bed	Entire bed domain
cool	Cooling
eff	Effective
ex	Exergy
g	Gas phase/air
i	Discretized calculation
o	initial
out	Out of control volume
rad	Radiation
s	Solid phase/sand
th	Thermal heat

1. Introduction

Applied smouldering systems harness a slow, flameless form of combustion and are emerging as a novel waste-to-energy technology to treat challenging wastes with limited alternatives – such as hazardous hydrocarbon waste liquids and contaminated soil [1–3]. One commercial application of these systems is referred to as Self-sustaining Treatment for Active Remediation ex situ (STARx), which uses batch processing to treat hydrocarbon-contaminated soil or hydrocarbon wastes (e.g., coal tar and waste oil sludges) intentionally mixed with an inert porous medium (e.g., sand or soil) [4–6].

Smouldering can be self-sustaining under a wide range of practical conditions (e.g., waste concentration, waste type, air flux) [7]. Smouldering treatment systems are generally highly applicable for challenging wastes that exhibit high moisture content, like sewage sludge, and/or low volatility, like oil sludge [6,8]. More recently, commercial smouldering systems as are emerging as a highly effective treatment technology for soils contaminated with per- and polyfluoroalkyl substances (PFAS), where high bed temperatures (>900 °C) are used to destroy PFAS [9,10]. These elevated temperatures highlight PFAS treatment applications as strong candidates for WHR implementation.

The term "self-sustaining" defines the condition where the rate of energy production is higher (i.e., heat released from oxidation) than the rate of local heat losses (e.g., to endothermic reactions, like pyrolysis, or heating up nearby waste or porous media). Therefore, an external heat source is only needed for ignition, as the subsequent smouldering process is sustained by the heat evolved from the oxidation reactions. As a result, applied smouldering treatment is highly energy efficient and ranks exceptionally well in quantitative sustainability assessments against alternative treatment options [4].

In application, the contaminated mixtures are loaded onto a treatment base (see Fig. 1A). Heating and air injection equipment in the base are used to ignite and sustain smouldering [5,11]. The heating equipment (e.g., electric radiative heaters) apply a localized heat flux at the base of the bed, raising the temperature of local contaminants/wastes to the ignition temperature, thereby producing the smouldering front that travels through the bed to drive treatment.

The air injection system supplies oxidizer (i.e., oxygen in the air) to the front and facilitates forward convection of the heat released from smouldering. Convective heat transfer drives upward smouldering propagation towards the top of the treatment bed (Fig. 1B). As the front travels – typically at average velocities around 0.4–0.6 m per day [5,11] – it removes virtually all contaminants and/or wastes within the bed, and therefore drives a very robust treatment method [5,11,12]. Treatment completes when the smouldering front reaches the top of the bed (Fig. 1B) and terminates (i.e., as virtually all fuel is consumed).

After treatment, only the hot, clean, inert porous medium remains. Average bed temperatures typically range from 500 to 1250 °C depending on many factors, including the concentration and type of waste being treated and the air flux applied [6]. Prior to the next treatment cycle, the hot clean bed must be cooled sufficiently to a "safe-to-manage" temperature (i.e., the "cooling phase") (Fig. 1B). This cooling phase may last several days based on system size and air flux [4,13]. Convection from air flux applied in the base produces hot gas out of the bed and is exhausted as "waste heat" in current applications. There is therefore an opportunity for waste heat recovery (WHR) methods to

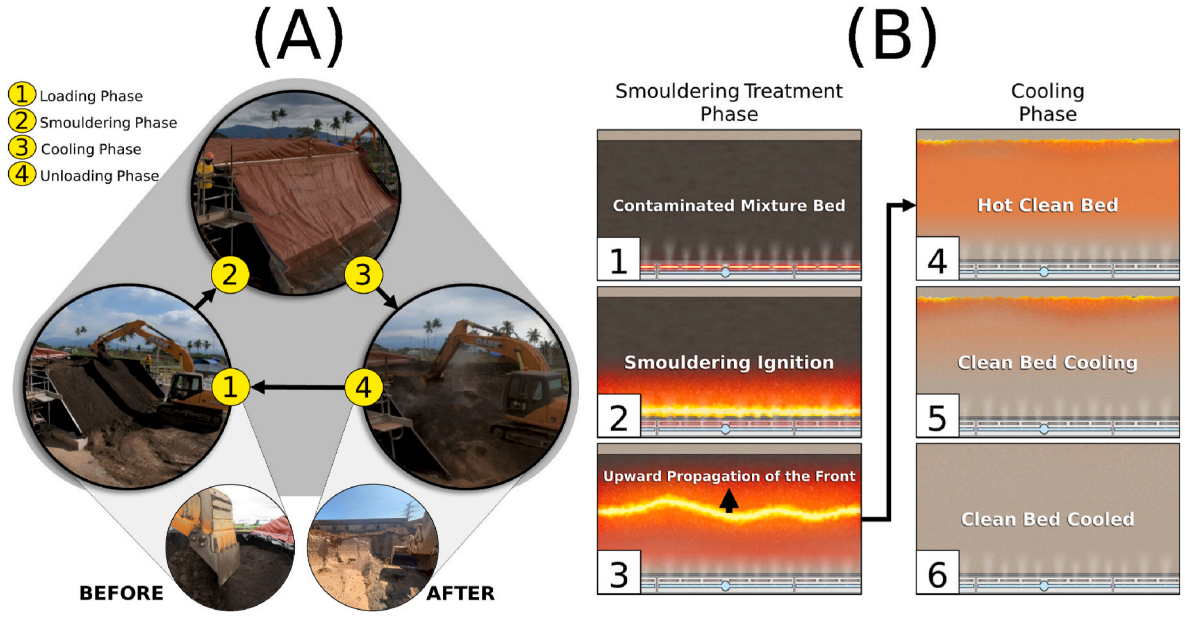

Fig. 1. (A) Outline of a typical smouldering treatment cycle as well as a comparison of the porous bed material BEFORE and AFTER treatment. (B) The general progression of the smouldering and cooling phases.

enhance smouldering applications through incorporating various technologies including recuperators and regenerators.

Recuperators are heat exchangers between exhaust and input process gases [14] (see Fig. 2A). Recuperators are suitable for low to high temperature applications and are used industrial furnaces, ovens, and steam boilers [14]. While recuperators promote gas-gas heat exchange, regenerators heat exchangers use gas-solid heat transfer. That is, waste heat is transferred to the porous matrix, which then heats up a separate cold stream. The cold stream is heated and exits the regenerator can be used as a heat source in other processes. Regenerators are used for WHR in glass and steel furnaces, coke ovens, and gas turbines see Fig. 2B [14].

Like regenerators, smouldering beds undergo alternating periods of charging and discharging. That is, energy accumulates in the porous bed during the smouldering phase, which is then discharged via the cooling phase. One WHR strategy could be to use the hot emissions from cooling smouldering beds to provide energy to support smouldering treatment in adjacent beds (Fig. 2C). This strategy is viable for existing operations that use multiple smouldering systems in sequence to treat batches of material, which effectively yields an overall continuous treatment process [4,15,16]. Therefore, the energy extracted from one system would not need to be stored temporarily but could be used to directly support a neighbouring system's smouldering phase. Moreover, the energy storage and outlet energy exhaust rates are highly controllable in these systems. For example, injection air can be stopped during cooling to increase the energy storage duration in the hot sand. Conversely, this air can also be increased to raise the output energy exhaust rate – as it is controlled by the cooling velocity in Equation (11). Therefore, it is possible to match temporal fluctuations between the waste heat availability and the waste heat needs in neighbouring systems.

While WHR methods are not yet implemented in application, there are relevant prototypes and emerging research that demonstrate opportunities for energy recovery from smouldering systems. For example, Shi et al., [17] has shown how energy may be harvested from coal fires – both for electricity production and for fire suppression. In a separate context, novel reactor designs from Duque et al., [18,19], Bittencourt et al., [20], and Pan et al., [21–23] have shown how excess energy from smouldering can be used to drive pyrolysis in nested reactors. Moreover, Bittencourt et al., [24] demonstrated how the hot porous media remaining after smouldering treatment can be harnessed to both (*i*) drive emissions treatment – as the hot bed during cooling could be used to combust hazardous products of incomplete combustion (such as unburned volatiles) and also (*ii*) support carbon capture with calcium based amendments. While these studies certainly show viable energy recovery methods, they are not easily integrated with current applied smouldering systems deployed commercially [4,5,11,15]. Instead, current systems would benefit from energy recovery techniques from the exhaust emissions after smouldering treatment.

Numerous smouldering-related academic papers have indicated the potential for energy recovery from exhaust gas [25–27]. However, to date, the recoverable energy from applied smouldering systems has not been quantified in the context of operational systems, let alone implemented. Commercial applied smouldering systems currently being deployed globally can be improved considerably via implementing energy recovery schemes. At commercial scale, energy recovery schemes can improve the operation's energy efficiency and economic competitiveness.

This work represents the first investigation into the potential for WHR from applied smouldering systems. A novel three-dimensional numerical model was developed to simulate the air flow and heat transfer dynamics in a commercial smouldering system's cooling phase – i.e., the timeframe in commercial operations that presents the most straightforward potential for energy recovery. The key objective of this study was to simulate system cooling dynamics that are not routinely measured in commercial practice but will govern WHR viability. Data available from a commercial application were used to capture the initial temperature and boundary conditions. The cooling dynamics in the

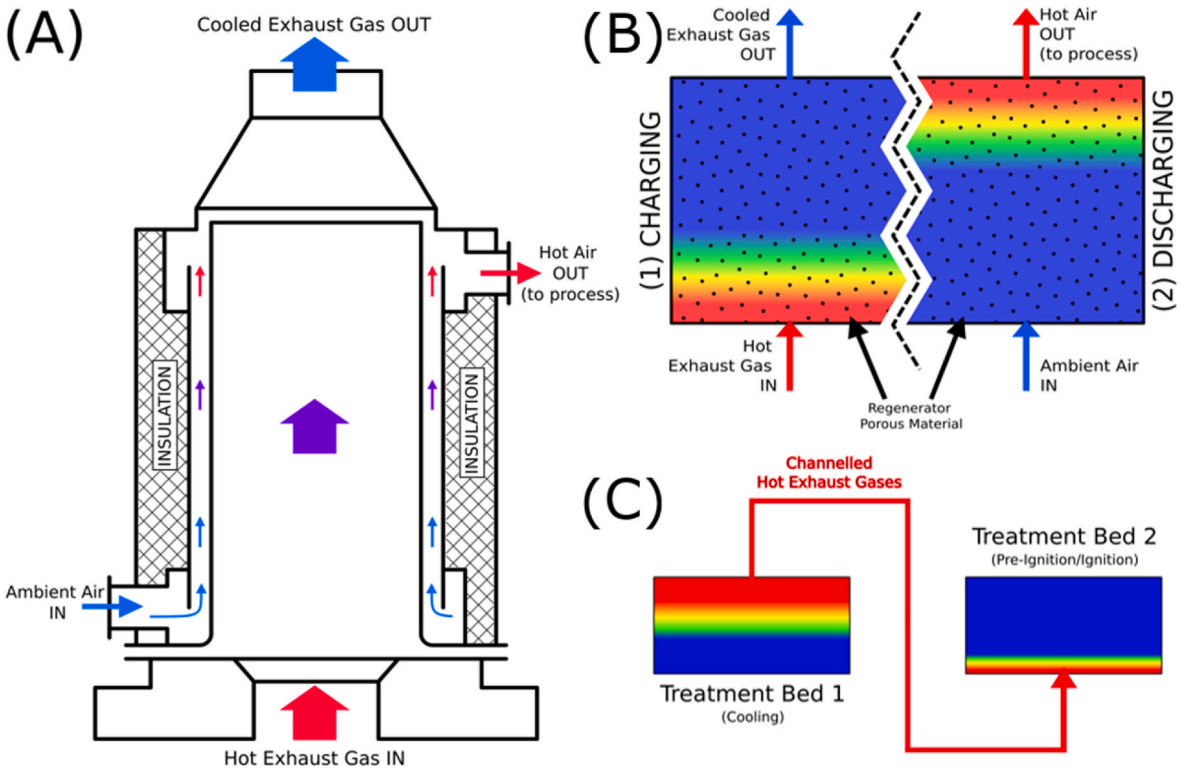

Fig. 2. (A) A schematic of a metallic radiation recuperator (adapted from Ref. [14], with permission from Elsevier). (B) A generalized schematic of a fixed bed/static-type regenerative heat exchanger. (C) A conceptual diagram of waste heat recovery between two smouldering treatment beds, where Treatment Bed 1 is in the cooing phase and Treatment Bed 2 is in the smouldering phase.

fixed bed were explored alongside the resulting waste heat exhausted as hot gases from system. This waste heat was quantitatively evaluated in terms of temporal availability and quality (i.e., via an exergy analysis). This study also investigated how temperature inhomogeneities within the fixed bed influenced waste heat recovery. Ultimately, this study provides novel insight that supports the progression of WHR methods for applied smouldering systems and other thermal fixed bed systems.

2. Material and methods

ANSYS® Student Fluent 2020 R2 was used in all simulations. This study applied a similar approach as proposed by Rashwan et al., [26,28] to assess global energy balance dynamics. As the cooling phase simulated was following smouldering treatment, no chemical reaction terms were applied. A three-dimensional model was necessary to simulate inhomogeneities that resulted from non-uniform smouldering treatment, common to applied smouldering systems. Only key modelling features are highlighted here as details on the model formulation can be found in Refs. [15,29].

2.1. Model formulation

2.1.1. Governing equations

The airflow was assumed to be incompressible and laminar due to small Mach and Reynolds numbers, respectively, which are common in smouldering systems [30]. The ideal gas law and Darcy's law were used to simulate mass and momentum conservation equations in Equations (1) and (2), respectively [31].

$$\frac{\partial(\phi\rho_g)}{\partial t}+\nabla\cdot\left(\rho_g q_g\right)=0 \tag{1}$$

$$q_g=-\frac{k_{int}}{\mu_g}\left(\nabla P+\rho_g g\right) \tag{2}$$

where, q_g is the Darcy flux, ϕ is the porosity, k_{int} is the intrinsic permeability, μ_g is the gas dynamic viscosity, ∇P is the pressure gradient, and g is gravity acceleration. The gas density was solved as $\rho_g = M_w P/R\,T_g$, where M_w is the molecular weight of air, R is the ideal gas coefficient, and T_g is the gas temperature.

Local Thermal Non-Equilibrium (LTNE) was assumed following methodology from Zanoni et al., [32]. LTNE was necessary to simulate because cooling in these systems is fundamentally driven by local phase temperature differences between the solid (i.e., sand) and gas (i.e., air) phases [6,26,33]. Equations (3) and (4) represent the solid- and gas-phase energy equations, respectively:

$$\frac{\partial}{\partial t}((1-\phi)\rho_s e_s)=\nabla\cdot((1-\phi)[k_s+k_{rad}]\nabla T_s)+h_{sg}A_{sg}\left(T_g-T_s\right) \tag{3}$$

$$\frac{\partial}{\partial t}\left(\phi\rho_g e_g\right)+\nabla\cdot\left(q_g\rho_g e_g\right)=\nabla\cdot\left(\phi k_g\nabla T_g\right)+h_{sg}A_{sg}\left(T_s-T_g\right) \tag{4}$$

where ρ_s is the solid particle density; e_s and e_g are the local solid and gas specific energies, respectively, solved as $e_s=\int_{T_{amb}}^{T_s} C_{ps}\,dT$ and $e_g=\int_{T_{amb}}^{T_g} C_{pg}\,dT$; T_s and T_{amb} are the solid and ambient temperatures, respectively; C_{ps} and C_{pg} are the solid and gas specific heat capacities, respectively; k_s, k_g, and k_{rad} are the thermal conductivities of the solid, gas, and solid radiative component following the Rosseland approximation (i.e., $k_{rad}=16\sigma d_p T_s^3/3$, where d_p is the solid particle diameter and σ is the Stefan-Boltzmann constant), respectively; h_{sg} is the solid-gas heat transfer coefficient, A_{sg} is the specific surface area of the solid-gas interface (i.e., $A_{sg}=6(1-\phi)/d_p$). Note h_{sg} was calculated using a correlation from correlation from Zanoni et al., [32] that related the Nusselt (Nu), Prantl (Pr), and Reynolds (Re) numbers, i.e., $Nu = h_{sg}d_p/k_g = 0.001\left(Re^{0.97}\,Pr^{1/3}\right)$, which is applicable for most applied smouldering systems [6]. The values assigned to all parameters and material properties are summarized in Table 1.

2.1.2. Computational domain and boundary conditions

Fig. 3A and B show the grid constructed to match the commercial treatment system simulated with 81 900 equally sized hexahedral elements chosen to balance accuracy with computational efficiency. Note that commercial smouldering systems in operation currently follow the generic design similar to the system shown in Fig. 3 [5,16,34,35]. As commercial smouldering systems are designed to be easily scalable to target treatment volumes, the primary geometric changes between systems are simply due to increases/decreases in the system's overall dimensions (i.e., length, width, and height). Therefore – while our study modelled specific aspects relevant to one commercial operation – that system was broadly representative of many current operational scales. In addition, the methodology below to quantify the potential energy from the emissions is relatively general and can be applied to analyze energy recovery potential from various other smouldering reactor orientations – e.g., with cylindrical reactors [36–38].

A constant 1 cm s^{-1} Darcy flux (q_g) at ambient temperature was simulated at the base of the bed that mimicked cooling protocols used in commercial application. The exhaust cooling gas then enters a "hood space" prior to an emissions treatment system. This space was covered and partially open to the environment; therefore, a constant zero-gauge pressure was applied at the top of the domain. No-slip flow conditions, and zero heat flux in the gas phase were applied at all containment walls.

In the solid-phase equations, no heat flux boundaries were used at the top and bottom of the domain and constant ambient temperatures were assumed at the containment walls. Note that these walls were not insulated and did not experience significantly hot temperatures. See the boundary conditions summarized in Table 2 and additional details in the Supplementary Materials.

2.1.3. Bed temperature distribution at the start of the cooling phase

Fig. 4 shows the temperatures measured from a commercial application that were used as the initial temperatures in the simulations (detailed in Supplementary Materials). All temperatures were measured with Type K thermocouples and exhibited a measurement error ≤4 % [28]. Note that temperatures were not recorded during the cooling phase; therefore, the initial temperatures represent the distribution at the end of the smouldering phase.

Table 1
Cooling phase simulation parameter set.

Parameters	Values	Source	Units [SI]
C_{pg}	$-3\times10^{-5}\left(T_g^2\right)+0.2261T_g+940.35$	[32]	[J kg^{-1} K^{-1}]
C_{ps}	$2.49T_s+39.06$		[J kg^{-1} K^{-1}]
k_g	$-1\times10^{-8}\left(T_g^2\right)+8\times10^{-5}\left(T_g\right)+4.3\times10^{-3}$		[W m^{-1} K^{-1}]
$k_{rad}+k_s$	$1.55\times10^{-10}(T_s^3)+0.000541(T_s)+0.1044$		[W m^{-1} K^{-1}]
μ_g	$-9\times10^{-12}\left(T_g^2\right)+4\times10^{-8}\left(T_g\right)+6\times10^{-6}$		[Pa s]
k_{int}	1.84×10^{-10}		[m^2]
ρ_s	2635		[kg m^{-3}]
d_p	5.125×10^{-4}		[m]
ϕ	0.37		[-]
P_{amb}	101 325	*ANSYS® Fluent Default Values*	[Pa]
R	8.31434		[J mol^{-1} K^{-1}]
M_w	0.029		[kg mol^{-1}]
T_{amb}	298.15		[K]
q_g	0.01	[13]	[m s^{-1}]

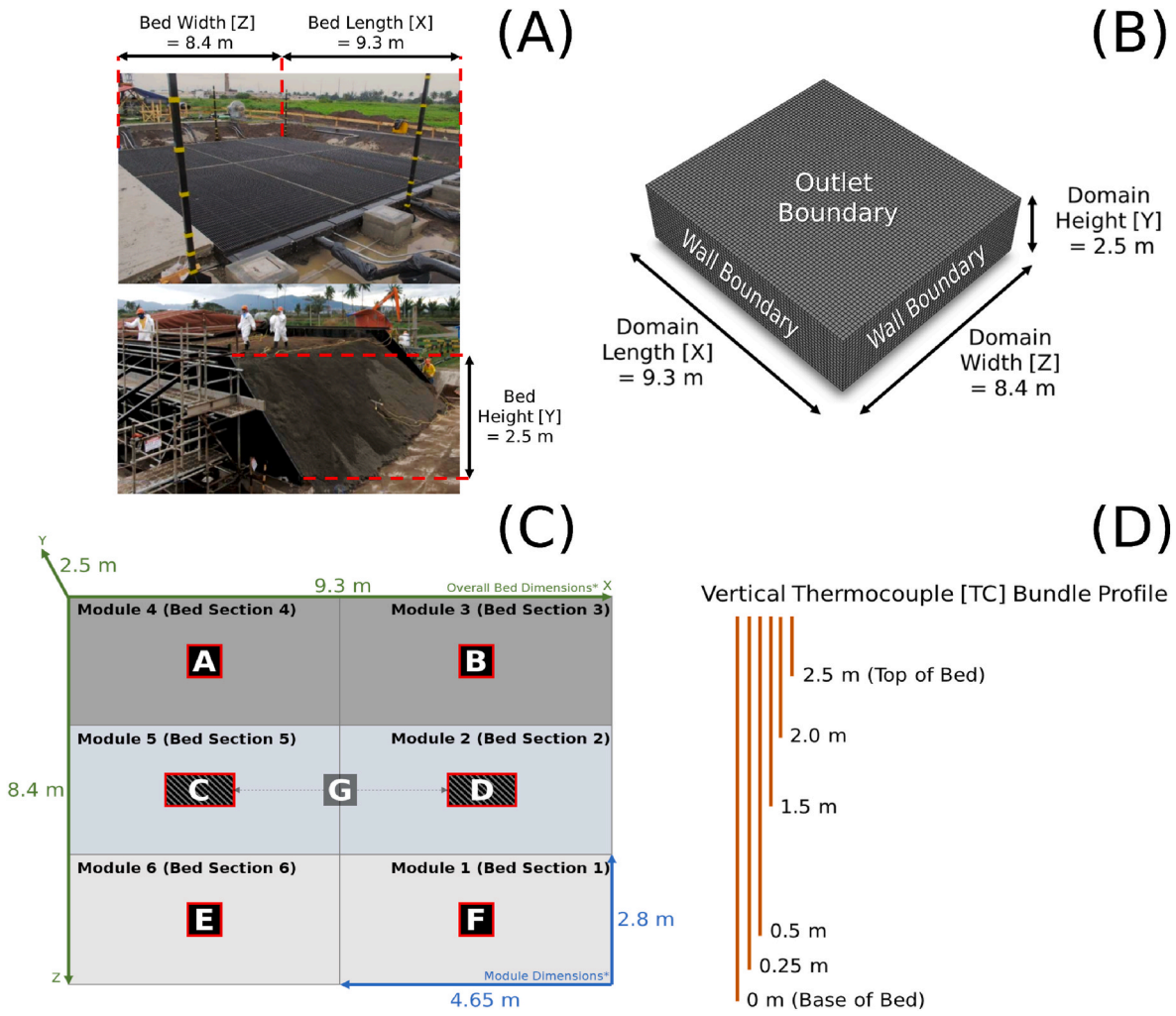

Fig. 3. (A) Photos and dimensions of the commercial treatment system. (B) Computational domain. (C) Top-down schematic view of the commercial treatment system. Lettered boxes outlined in red indicate the thermocouple (TC) bundles. (D) The profile of vertical temperature measurements for TC bundles.

Table 2
Summary of cooling phase simulation boundary conditions.

Boundary Type	Position	Momentum Conditions	Thermal Conditions	
		Gas Phase	Gas Phase	Solid Phase
Velocity Inlet	$y = 0\,m$ $-4.65\,m \le x \le 4.65\,m$ $-4.2\,m \le z \le 4.2\,m$	0.01 m s^{-1}	Constant 25 ° C	Zero Heat Flux
Wall (Right)	$0\,m \le y \le 2.5\,m$ $x = 4.65\,m$ $-4.2\,m \le z \le 4.2\,m$	Stationary wall X,Y zero shear	Zero Heat Flux	Constant 25 ° C
Wall (Left)	$0\,m \le y \le 2.5\,m$ $x = -4.65\,m$ $-4.2\,m \le z \le 4.2\,m$			
Wall (Front)	$0\,m \le y \le 2.5\,m$ $-4.65\,m \le x \le 4.65\,m$ $z = 4.2\,m$			
Wall (Back)	$0\,m \le y \le 2.5\,m$ $-4.65\,m \le x \le 4.65\,m$ $z = -4.2\,m$			
Pressure Outlet	$y = 2.5\,m$ $-4.65\,m \le x \le 4.65\,m$ $-4.2\,m \le z \le 4.2\,m$	0 Pa (Gauge)	Constant 25 ° C	Zero Heat Flux

Following the methodology from Morales et al., [15], a cool edge near the walls was used to account for edge effects from heat losses near the walls during smouldering treatment. Physically, this assumption represents a crust that is commonly formed near to the walls of these systems due to unburned material near the walls [11]. This region was set as 0.2 m around the system perimeter from walls inwards and was initially at 40 °C. Though the wall temperatures were not explicitly measured in the application because of limited temperature measurements (see Fig. 3), this assumption is generally representative of wall temperatures and crust commonly observed in application [11,13]. Fig. 4B shows the initial temperatures from TCs, where the initial volume-averaged temperature was ~262 °C. The temperature distributions in Fig. 4B are characteristic of real-system heterogeneities that are from smouldering non-uniformities during treatment (e.g., due because of fuel and moisture heterogeneity) [11,39]. The commercial system also operated with an ignition sequence where different bed sections were ignited sequentially so to limit the peak energy needed for ignition. This sequential ignition led to additional temperature non-uniformities at the start of the cooling phase.

2.2. System energy consumption for smouldering treatment

The energy consumption used for ignition was estimated from the total system energy usage, which was largely governed by the air injection and ignition heaters [5,13,34]. Fig. 5 shows the total system

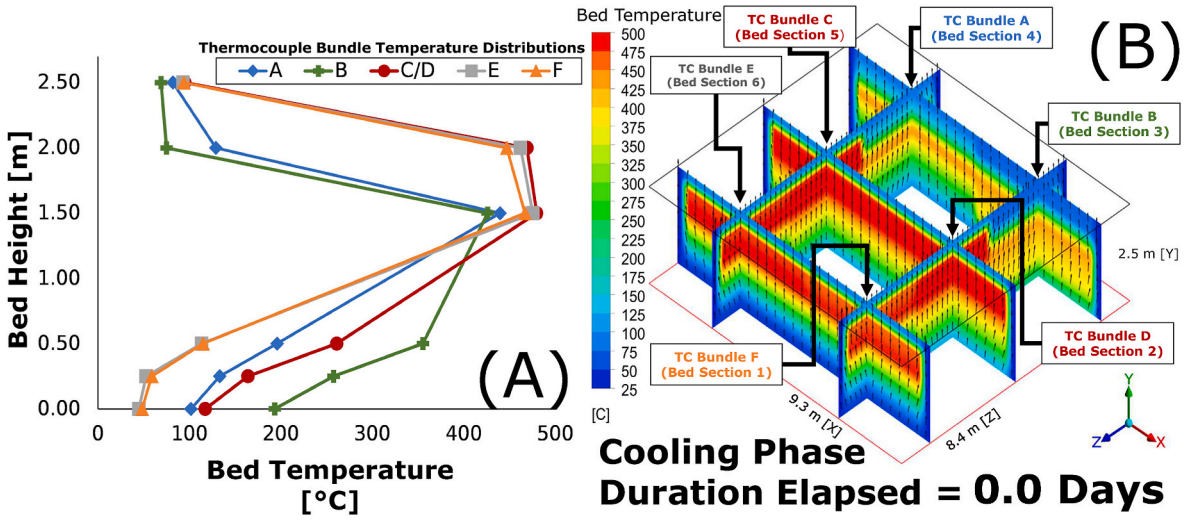

Fig. 4. (A) The initial temperatures used from each bed section, i.e., sections A-F shown in Fig. 3. (B) The initial temperatures shown on 2D-planes.

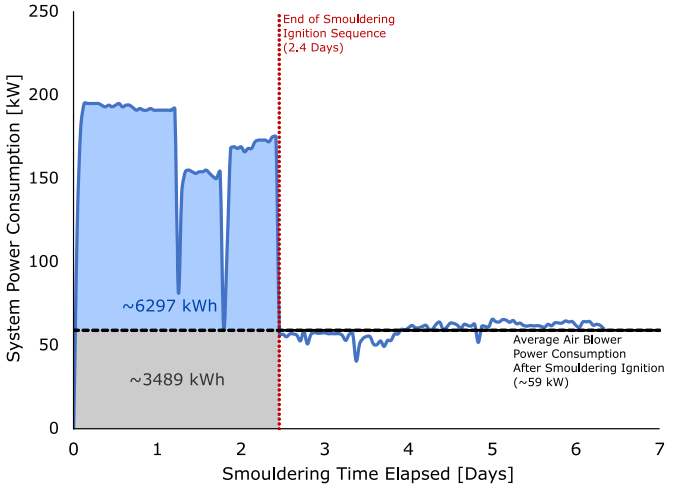

Fig. 5. System power consumption during the smouldering phase. The end of the smouldering ignition is indicated with a red dashed line (after 2.4 days) and the average air injection power consumption is indicated with a black solid line (~59 kW). The 6297 and 3489 kWh note the approximate total energy usage from the heaters and air injection equipment during the ignition phase, respectively. Adapted from Murray [13].

energy usage over the treatment phase, where the total energy usage over the treatment time was integrated as 15 100 kWh. Note that the end of the ignition period is clearly seen after 2.4 days (i.e., when the ignition heaters were turned off). The air injection equipment drew roughly constant energy usage after ignition (~59 kW) for the constant air flow over the full operation. This consumption was integrated over the ignition duration as ~3498 kWh during ignition. The remaining energy usage during this period was due to the heaters for ignition, which was estimated as ~6297 kWh, i.e., approximately 42 % of total system energy consumption during treatment.

2.3. Model validation and verification

The model verification and validation procedure followed the same methodology detailed in Morales et al., [15]. For verification, a mesh convergence study confirmed that spatial and temporal discretization were acceptable, and results were grid independent [15]. As stated above, cooling phase temperatures from the commercial application were not available for validation. That is, temperature data was only collected until the end of smouldering treatment. Therefore, although this data could be used to set the initial bed temperature distribution at the start of cooling (i.e., the end of smouldering), temperature data throughout the cooling was not available for model validation. Consequently, the model was validated against available cooling phase data from a published laboratory smouldering experiment from Zanoni et al., [31]. All temperatures were measured with Type K thermocouples and exhibited a measurement error $\leq$1 % [28]. A 2D axisymmetric model was developed for validation that represented a typical laboratory smouldering column, which used the same representative elementary volume-scale assumptions as the main 3D model. Cooling phase temperatures from the experiment and the simulation were compared at centerline (Fig. 6A) and near to the column wall (Fig. 6B). The Normalized Root-Mean-Square Deviation between the experiments and simulations was very low, near 7 % [15].

Overall, this validation procedure provides confidence that the model properly simulates the key cooling dynamics (i.e., with no complex smouldering-related reactions or energy sources/sinks). As such, the governing equations are not altered due to changes in system scale. Therefore, the governing equations can be properly applied to a range of smouldering system scales to simulate post-smouldering bed cooling, such as the lab and commercial scales that were considered in this validation procedure.

The novelty of this model entails some limitations. For instance, the influence of some boundary conditions may warrant further examination. While previous investigations into scalability broadly support the boundary conditions applied in this study [26,40,41], a direct validation would be highly valuable. That validation was not completed in this study due to data unavailability.

2.4. Calculations

2.4.1. Cooling phase duration

The "cooling phase duration" is the time available for WHR in typical smouldering operations. That is, this is the time from the end of treatment until the volume-averaged bed temperature reaches 60 °C, which is the safe-to-manage temperature.

2.4.2. Waste heat quantity

The waste heat quantity is the total thermal energy from the hot gas flow during the cooling duration. This waste heat quantity rate $(\dot{E}_{g,out})$ and total $(E_{g,out})$ were estimated following Equation (5):

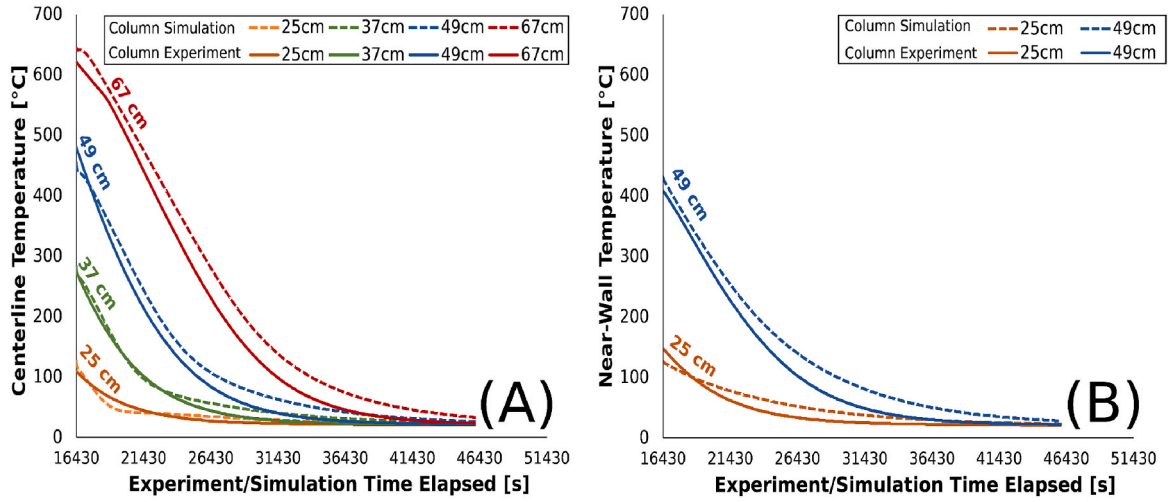

Fig. 6. Simulated (dashed lines) and experimental (solid lines) temperatures at different column locations: (A) at the centerline and (B) near the column wall.

$$\dot{E}_{g,out} = \sum_{i=1}^{n_{out}} e_{g,i}\rho_{g,i}q_{g,i}A_i$$
$$E_{g,out} = \int_{t_o}^{t_{cool}} \dot{E}_{g,out}dt \quad (5)$$

where i notes the cell face and the total number of cells at outlet boundary is n_{out}. The beginning and end of the cooling times are noted with t_o and t_{cool}, respectively, and A_i is the cell area.

2.4.3. Waste heat quality

The waste heat quality was calculated as the exergy from the hot gas during cooling. As described above, applied smouldering systems' energy usage is dominated by electrical energy needed for air injection and ignition. Therefore, one pathway for WHR is to use this waste heat to offset these usages and an exergy analysis can provide insight into this potential. Therefore, the exergy rate $(\dot{\Xi}_{g,out})$ and total $(\Xi_{g,out})$ were calculated following [42]:

$$\dot{\Xi}_{g,out} = \sum_{i=1}^{n_{out}} \rho_{g,i}q_{g,i}A_i\left(\int_{T_{amb}}^{T_{g,i}} C_{pg,i}\left(T_{g,i}\right)dT - T_{amb}\int_{T_{amb}}^{T_{g,i}} \frac{C_{pg,i}\left(T_{g,i}\right)}{T_{g,i}}\,dT\right)$$
$$\Xi_{g,out} = \int_{t_o}^{t_{cool}} \dot{\Xi}_{g,out}dt \quad (6)$$

Equation (6) shows how the exergy increases with temperature as higher temperature sources are of higher quality greater potential for work. Waste heat is often categorized into "grades" of quality for convenience as low, medium, and high waste heat qualities. Generally, waste heat at ≤ 200–250 °C and ≥400–650 °C typically correspond to low- and high-grade sources, respectively, where medium-grade sources are between these temperature ranges [14].

To estimate the waste heat grade simulated, the mass-averaged exhaust gas temperature was calculated at each timestep:

$$\overline{T}_{g,out} = \frac{\sum_{i=1}^{n_{out}} T_{g,i}\rho_{g,i}\left|q_{g,i}A_i\right|}{\sum_{i=1}^{n_{out}} \rho_{g,i}\left|q_{g,i}A_i\right|} \quad (7)$$

The results from Equation (7) were averaged over the cooling duration and to define a grade. The exhaust gas temperatures were captured at the top outlet boundary (see Fig. 3B). In application, exhaust gas temperatures would be slightly cooler than these simulated temperatures because of heat losses and ambient air mixing in the hood space. Additionally, ambient temperatures will affect viable waste heat recovery opportunities discussed in Section 1. Higher ambient temperatures will reduce the temperature difference driving recovery and reduce the exergy availability. Therefore, waste heat recovery from commercial smouldering systems operating in high-temperature climates will be more challenging to operate.

2.4.4. Wall heat losses

During cooling, some heat was lost through lateral heat transfer out of the bed walls, where the energy loss rate $(\dot{E}_{wall,out})$ and cumulative lost energy $(E_{wall,out})$ were calculated from the solid energy results with Equation (8) as:

$$\dot{E}_{wall,out} = \sum_{i=1}^{n_{wall}} \frac{k_s}{\Delta n_{wall}}\left(T_w - T_s\right)$$
$$E_{wall,out} = \int_{t_o}^{t_{cool}} \dot{E}_{wall,out}dT \quad (8)$$

where T_w is the wall temperature, n_{wall} is the total number of near-wall cells, and Δn_{wall} is the distance from the near-wall cells to edge of the model.

2.4.5. Sensible heat storage

The sensible heat storage was determined from the simulated hot solids as:

$$E_{bed} = (1-\phi)\sum_{i=1}^{n_{bed}} e_{s,i}\rho_{s,i}V_i \quad (9)$$

where, n_{bed} is the total number of cells, V_i is the volume of cell i. Equation (9) provides a quantification of the maximum energy recoverable through WHR. Equation (10) describes the stored thermal exergy in the bed:

$$\Xi_{bed} = (1-\phi)\sum_{i=1}^{n_{bed}} \rho_{s,i}V_i\left(\int_{T_{amb}}^{T_{s,i}} C_{ps,i}\left(T_{s,i}\right)dT - T_{amb}\int_{T_{amb}}^{T_{s,i}} \frac{C_{ps,i}\left(T_{s,i}\right)}{T_{s,i}}\,dT\right) \quad (10)$$

2.4.6. Cooling velocity

During the smouldering system's cooling phase, the key cooling dynamics are captured in the characteristic cooling front velocity (i.e., the rate that the cooling wave travels through the bed). Relatedly, the system's rate of cooling (or the rate of thermal energy storage decrease) is proportional to the characteristic cooling front velocity.

To explore these cooling features, the cooling velocity (v_{cool}) of the commercial smouldering application was calculated by Equation (11),

which essentially solves for an energy balance across the cooling front [26,43]:

$$v_{cool} = \frac{\rho_g C_{pg_{eff}}}{\phi \rho_g C_{pg_{eff}} + (1-\phi)\rho_s C_{ps_{eff}}} q_g \quad (11)$$

where $C_{pg,eff}$, and $C_{ps,eff}$ are the effective specific heat capacities of air and sand, respectively. Following Rashwan et al., [26], these effective specific heat capacities were estimated as $\rho C_{p_{eff}} = \int_{T_{amb}}^{T_{peak}} \rho C_p(T) dT / (T_{peak} - T_{amb})$, where T_{peak} is the peak bed temperature at the start of cooling (480 °C, see Section 2.1.3) and T_{amb} is the ambient temperature (25 °C).

The total amount of energy available for recovery will ultimately be related to the total waste in the system. Increased packing will increase the waste mass in the system and energy available for recovery. Because commercial systems are not highly affected by heat losses [26,28,41], the total energy available for recovery (E_{bed}) will roughly equal the amount of heat released and stored in the bed during the smouldering phase, i.e., $E_{bed} \approx \Delta H m_{waste}$, where ΔH is the heat released per mass of waste and m_{waste} is the total mass of waste. Increased packing will also affect the utilization prospects, as the rate of heat transfer will decrease as porosity decreases, as seen in the cooling velocity in Equation (11). That is, increased packing will decrease the porosity, slow the cooling velocity, and essentially slow the rate of energy recovery from the smouldering system.

3. Results and discussion

3.1. Cooling phase duration, energy storage & bed cooling dynamics

Based on volume-averaged bed temperature, the simulated cooling duration was ~4.1 days (Fig. 7A), which agrees with typical cooling times in practice [13,15]. Upon cooling, the total sensible heat stored was 25 912 kWh_{th} (Fig. 7A), which dropped to 3 359 kWh_{th} at the end of cooling, i.e., when the system reached an average of 60 °C. That is, about 13 % of the initial sensible heat remained within the bed at the end of cooling, as 86 % was exhausted. As shown in Fig. 7A, the entire system cooled to ambient temperatures after 7.1 days; therefore, an additional 3 days of cooling was needed to extract this remaining heat after reaching the average 60 °C. As the additional cooling time results in diminishing returns, the remaining heat after 4.1 days of cooling is effectively unrecoverable.

Fig. 7B shows the simulated hot exhaust gas was a medium-grade waste heat source, as it reached >250 °C for 63 % of cooling (i.e., 2.6 days). The gaussian profile of the exhaust gas temperatures is due to how the thermal wave travelled through the system. That is, the exhaust temperature increase seen in Fig. 7B corresponded with the leading edge of the thermal wave travelling through the bed up towards the top outlet of the system – as seen in Fig. 7C–E. The exhaust temperatures then dropped as the trailing edge of the thermal wave was driven via convection out the top of the bed in Fig. 7C–H. The scale analysis in Fig. 7B that relates the peak emissions temperature time (t_{peak}), cooling distance (x_{cool}) and the cooling velocity (v_{cool}) as $t_{peak} \sim x_{cool}/v_{cool}$ explains the temporal response in the peak emissions temperatures. That is, t_{peak} occurred after ~2 days of cooling as the peak bed temperatures travelled a cooling distance (x_{cool}) ~1 m (i.e., as the peak temperatures in Fig. 4 were all ~1 m from the top of the bed), and the cooling velocity (v_{cool}) was estimated as ~0.5 m day^{-1}, following Equation (11) – as discussed and shown below in Fig. 8. Videos of the bed temperature evolutions are provided as Supplementary Material.

Fig. 7C–H also show how cooling dynamics varied laterally over the bed. As described in Section 2.1.3, the initial bed temperatures shown in Fig. 7C resulted from smouldering treatment non-uniformities. These non-uniformities drove cooling differences. The air velocity quivers in

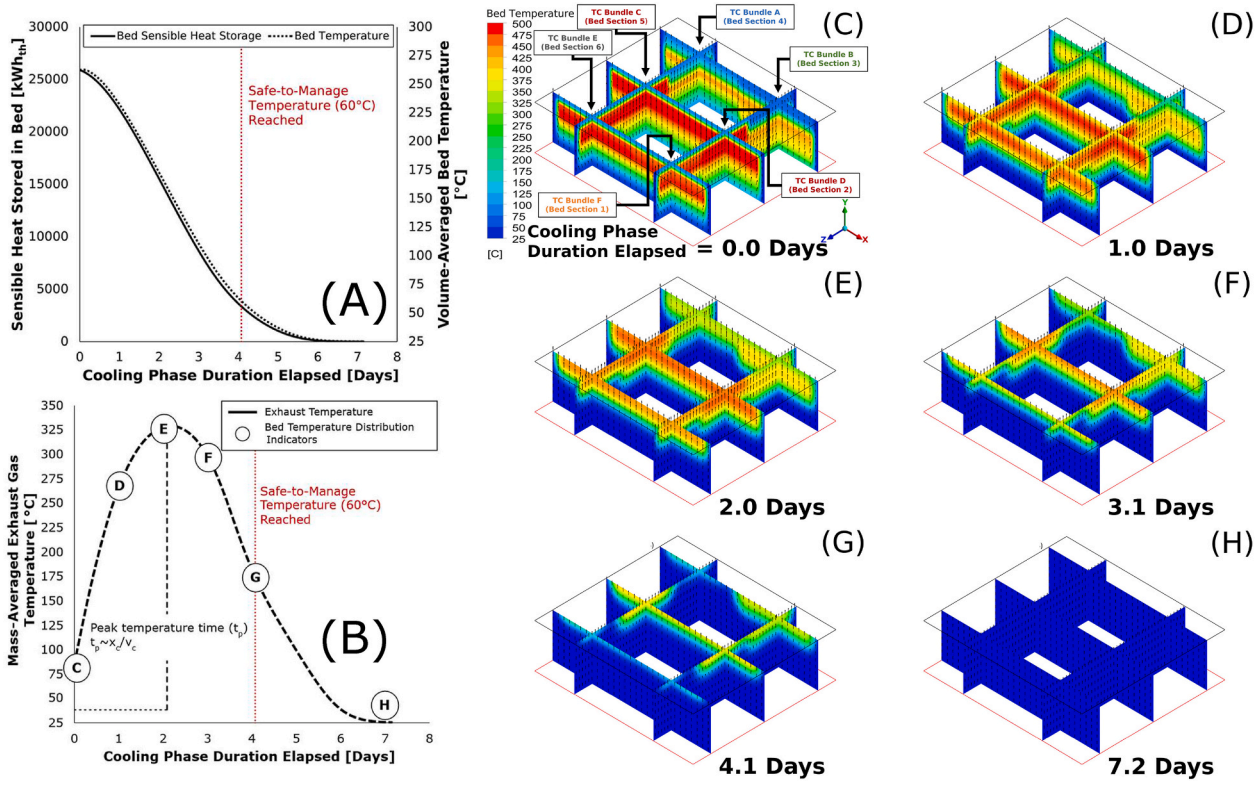

Fig. 7. (A) Bed temperature and sensible heat storage and (B) exhaust gas temperatures over the cooling phase. The markers in (B) correspond to the exhaust temperatures simulated at the times in (C)–(H). (C) start of cooling, (D) after ~25 % of cooling [1 day], (E) ~50 % of cooling [2 days], (F) ~75 % of cooling [3.1 days], (G) ~100 % of cooling [4.1 days] (i.e., end of the cooling phase), and (H) ~175 % of cooling [7.1 days] (i.e., at ambient temperature). The peak temperature time (t_{peak}) occurred at ~2 days, related to the cooling length (x_{cool}) and cooling velocity (v_{cool}).

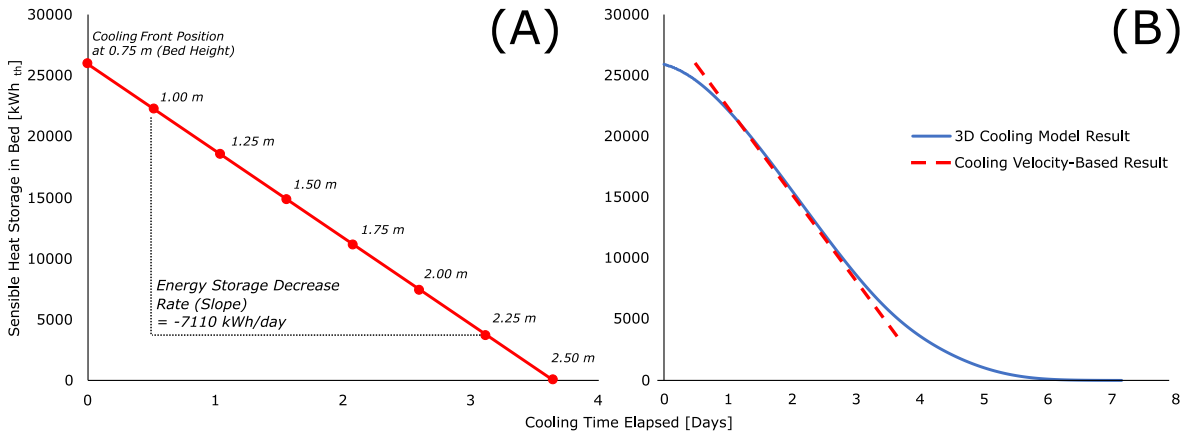

Fig. 8. (A) The progression of bed cooling based on the characteristic cooling front velocity-based model. The position of the transient position of the cooling front as well as the rate of energy storage decrease are indicated. (B) The comparison between the progression of bed cooling as determined by the 3D and cooling velocity-based models.

Fig. 7C–G show how air preferentially bypassed hot regions in the bed and therefore drove faster convection in the cooler regions. This bypassing, or non-uniform air flux, is due to the thermophysical properties of the air – principally due to air viscosity differences [15,30,31,44]. That is, air preferentially flows towards cooler regions with lower viscosity and lower flow resistance. Consequently, the cooler regions cooled faster than hotter regions. This effect can be seen as Bed Section 4 (i.e., the coolest section) cooled faster than other bed sections in Fig. 7C–G. These non-uniformities are important to capture because they lead to inefficiencies relevant to WHR. That is, non-uniform air flux leads to cooler exhaust gas temperatures and longer cooling phases – both of which inhibit energy recovery prospects. Therefore, multi-dimensional models, like the one presented here, are needed to forecast the potential for WHR from applied smouldering systems.

The cooling velocity (v_{cool}) was estimated to be 5.56 x 10^{-6} m s^{-1} (i.e., 0.480 m day^{-1}). The v_{cool} can then be used to explain the rate of thermal energy storage as:

(1) Transient energy storage is proportional to the movement of the cooling front.
(2) The bed is cooled to ambient temperature when the cooling front reaches the top of the bed.

The initial position of the cooling front was estimated as the midpoint between the bed heights where the maximum and minimum bed temperatures were observed (i.e., the midpoint of the initial vertical temperature gradient in the bed, in Fig. 4). From Fig. 4A, the peak temperature is at 1.50 m from the base (i.e., 480 °C, TC Bundles C and D). The coolest temperature is found at 0 m (i.e., 40 °C, in the cool edge). Therefore, the initial cooling front position was approximated at 0.75 m above the air inlet, which was 1.75 m below the top of the bed. Following point (1) above, energy storage was calculated at several bed heights, which track the upward movement of the cooling front (i.e., 0.75–2.50 m in Fig. 8). The change in energy storage can be plotted over time by using v_{cool} to track the cooling front position. Fig. 8 shows the results of this estimation, where the slope is the rate of bed energy storage decrease.

Fig. 8 overlays the result of the analytical v_{cool} analysis on the overall energy storage result from the 3D numerical model. This comparison highlights good alignment between the rates of energy storage decrease between the two models and provides: (*i*) additional verification that the 3D model was correctly developed and implemented; (*ii*) clarity on the fundamental heat transfer mechanisms driving cooling dynamics; (*iii*) insight into the overall impact of non-uniform air flux on the global cooling trends, which is seen as the tailing cooling curve from approximately 4-6 days. Fig. 8 illustrates that the potential rate of energy recovery is essentially governed by v_{cool}.

3.2. Waste heat quantity, quality, and temporal availability

Fig. 9 shows the evolution of the stored thermal energy and exergy over time in bed compared to the cumulative energy and exergy in the exhaust. The cumulative heat losses and exergy destruction dynamics are also shown. As shown in this figure, nearly all the stored energy was recoverable after 7.1 days, i.e., ~99 % of the stored energy was recoverable in the emissions – as cumulative heat losses only drew ~1 % from the bed's stored thermal energy. Over this time, ~55 % of the original exergy (13 753 kWh_{ex}) was destroyed, i.e., as only 7 602 kWh_{ex} was recoverable. However, over the practical WHR time frame, i.e., until 4.1 days, ~86 % of the initial sensible heat (i.e., ~22 168 kWh_{th}) and ~50 % (6 855 kWh_{ex}) was exhausted in the emissions during cooling and ~13 % remained practically unrecoverable (as discussed in Section 3.1 and shown Fig. 7). The exergy destruction shown in Fig. 9 was largely driven by temperature differences between the hot regions in the bed (i.e., up to 500 °C, Fig. 7C) and the cooler emissions temperatures, which peaked near 325 °C (Fig. 7B).

Fig. 10A isolates the thermal energy and exergy rates calculated from the exhaust during cooling. Like the exhaust gas temperatures in Fig. 7B, the thermal energy and exergy rates followed a gaussian profile, which peaked at 227 kW_{th} and 99 kW_{ex} at 2.1 days of cooling, respectively. For context, the power consumption during the smouldering treatment

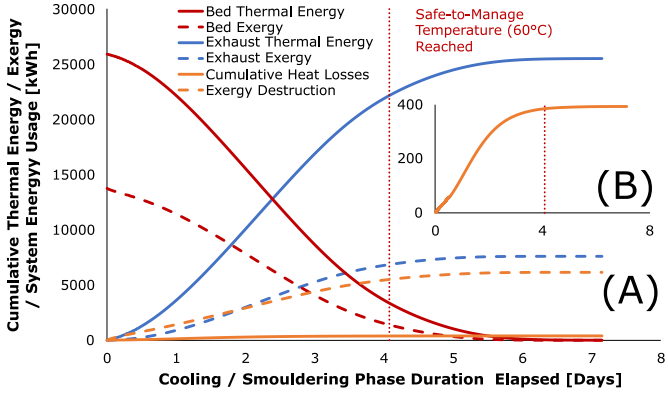

Fig. 9. (A) Bed thermal energy and exergy cumulative amounts compared to those in the exhaust. Cumulative heat losses and exergy destruction is also plotted. (B) Isolated plot of the cumulative heat losses profile, where the axis labels are common to (A).

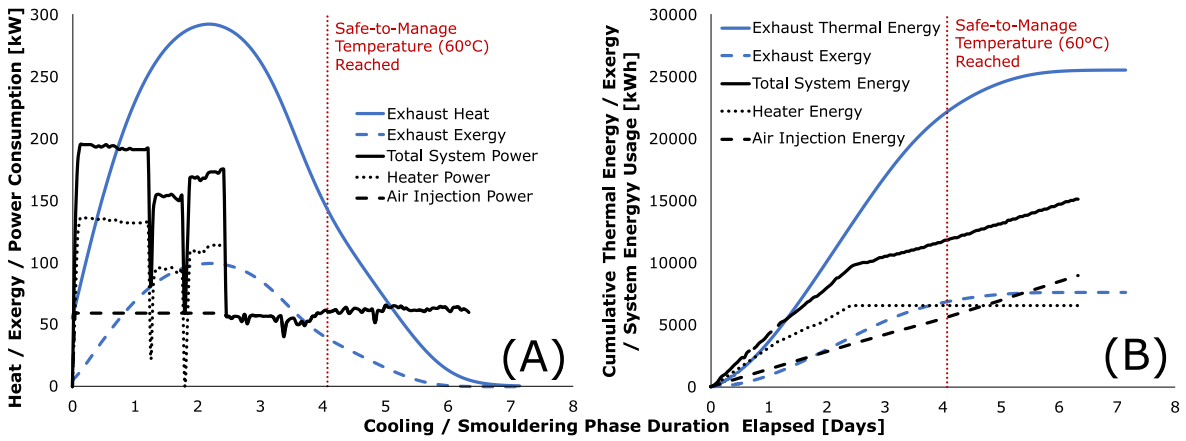

Fig. 10. (A) Exhaust heat and exergy rates during the cooling phase, alongside system power consumption during smouldering treatment phase. (B) Cumulative profiles from (A).

phase from Fig. 5 is overlain on Fig. 10A. The peak power consumption throughout treatment was ~150–195 kW during ignition and 59 kW after ignition (as discussed above in Section 2.2). Therefore, the exergy rates suggest that the exhaust emissions could be used during the treatment phase to offset a theoretical maximum of 50–66 % of the peak power during ignition (i.e., for heaters and air injection) and all energy needed after ignition (i.e., only for air injection).

Fig. 10B shows the cumulative thermal energy, exergy, and power consumption. As discussed in Section 2.2, the total electrical energy is separated into the amount approximately used for the air injection equipment (~60 %) and heaters (~40 %). The total recoverable thermal energy from cooling (~22 168 kWh_{th}) was ~1.5× the system's overall energy consumption during treatment (i.e., 15 100 kWh), whereas the total exergy from cooling was ~6 855 kWh_{ex} (Fig. 10B). Therefore, the output exergy during the cooling phase was 45 % of the cumulative electrical energy needed to drive equipment during the smouldering phase. As applied smouldering systems often operate with multiple parallel batch systems [4], WHR from one system cooling can be integrated to support a neighbouring system's treatment operations. Therefore, this analysis suggests that the energy recovery from cooling one system may be compatible with offsetting the air injection and/or heater energy needed in a neighbouring system.

Beyond supporting the energy needs for nearby system heaters and air injection equipment, waste heat could be use used for various other activities including (*i*) emissions treatment [24], or (*ii*) fuel preheating or endothermic pre-processing (e.g., fuel charring via pyrolysis to increase the energy density or pre-drying to decrease moisture content). The dual smouldering/pyrolysis reactors proposed in the literature may be advantageous for this purpose [18,22,45]. WHR methods that involve the direct reuse of waste heat can be advantageous due to their simplicity. Conversely, the external reuse of recovered waste heat (e.g., exporting electrical power produced from the conversion of waste heat) may be best when direct reuse is not feasible or practical. The selection of WHR methods and technologies is also consequential to the amount of energy that can be recovered. For example, heat exchanger design can greatly impact heat recovery efficiency. The selection of an effective use for the recoverable waste heat from smouldering systems is critical, but beyond the scope of this study's initial assessment. Overall, this investigation highlights the total recoverable thermal energy and exergy possible and puts these values in context of a system's energy consumption to support the progression and optimization of WHR in applied smouldering systems.

4. Conclusion

Smouldering treatment systems provide strong benefits in treating challenging wastes and are now deployed globally. However, these systems operate in a batch orientation, where the excess energy from smouldering is exhausted as hot gases during the cooling phase after treatment. This exhaust gas presents an opportunity for waste heat recovery. This research quantified this waste heat recovery opportunity and put the benefits into context of the energy needed through integrating a 3D numerical model with data from a commercial smouldering application for the first time. From an exergy analysis on the resulting exhaust gas, it was found that the cumulative output exergy during the cooling phase was 45 % of the cumulative electrical energy needed to drive equipment during the smouldering phase. While there are various recovery strategies that can be considered, both from a technical and economic perspective, this study provides new quantifications and insights to drive further recovery-focused research to improve the efficiencies of smouldering systems for environmentally beneficial purposes.

CRediT authorship contribution statement

Ryan B. Morales: Writing – original draft, Visualization, Validation, Software, Methodology, Investigation, Formal analysis, Data curation, Conceptualization. **Tarek L. Rashwan:** Writing – review & editing, Supervision, Methodology, Investigation, Funding acquisition, Formal analysis. **Marco A.B. Zanoni:** Writing – review & editing, Formal analysis. **Christopher T. DeGroot:** Writing – review & editing, Supervision, Methodology. **Jason I. Gerhard:** Writing – review & editing, Supervision, Resources, Project administration, Methodology, Investigation, Funding acquisition, Formal analysis, Conceptualization.

Declaration of competing interest

The authors declare the following financial interests/personal relationships which may be considered as potential competing interests: Geosyntec Consultants, Inc. - through its subsidiary Savron - holds an exclusive license to commercialize smouldering remediation technology. Ryan B. Morales is employed by Geosyntec Consultants, Inc.

Acknowledgements

Funding was provided by the Ontario Ministry of Research, Innovation, and Science; the Natural Sciences and Engineering Research Council of Canada (Grant Nos. CREATE 449311-14, RGPIN 2018–06464, and RGPAS-2018-522,602); the Royal Society (RG\R2 \232528); and the Open University through: (*i*) a Higher Education Innovation Funding Knowledge Transfer Voucher and (*ii*) the Open Societal Challenges Programme in support of the SPLICE challenge.

ANSYS® Student Fluent 2020 R2 was used for this research with approval from ANSYS Inc. We dedicate this paper in loving memory of our inspirational colleague, mentor, and dear friend, Prof. Jason Ian Gerhard.

Appendix A. Supplementary data

Supplementary data to this article can be found online at https://doi.org/10.1016/j.energy.2025.138527.

Data availability

Data will be made available on request.

References

[1] Gan Z, Deng L, Wang J, Cheng G, Zhao C, Zhang Z, Li Y, Song Z. Method of smoldering combustion for the treatment of oil sludge-contaminated soil. Waste Manage 2024;175:73–82. https://doi.org/10.1016/j.wasman.2023.12.048.

[2] Vidonish JE, Zygourakis K, Masiello CA, Sabadell G, Alvarez PJJ. Thermal treatment of hydrocarbon-impacted soils: a review of technology innovation for sustainable remediation. Engineering 2016;2(4):426–37. https://doi.org/10.1016/J.ENG.2016.04.005.

[3] Fu J, Zhang S, Ji L, Xu X, Jiao W, Chen T, Li X, Zhan M. State of the art in self-sustaining smoldering for remediation of contaminated soil and disposal of organic waste. J Hazard Mater 2024;474:134667. https://doi.org/10.1016/j.jhazmat.2024.134667.

[4] Gerhard JI, Grant GP, Torero JL. Chapter 9 - star: a uniquely sustainable in situ and ex situ remediation process. In: Hou D, editor. Sustainable remediation of contaminated soil and groundwater. Butterworth-Heinemann; 2020. p. 221–46.

[5] Sims AW, Sabadell GP, Lam CW, Segal DC, Bireta P, Thomas D. Self-sustaining smouldering combustion for the treatment of industrial oily waste. Waste Manag Res 2023;41(3):713–22. https://doi.org/10.1177/0734242x221123145.

[6] Torero JL, Gerhard JI, Martins MF, Zanoni MAB, Rashwan TL, Brown JK. Processes defining smouldering combustion: integrated review and synthesis. Prog Energy Combust Sci 2020;81:100869. https://doi.org/10.1016/j.pecs.2020.100869.

[7] Zanoni MAB, Torero JL, Gerhard JI. Delineating and explaining the limits of self-sustained smouldering combustion. Combust Flame 2019;201:78–92. https://doi.org/10.1016/j.combustflame.2018.12.004.

[8] Rashwan TL, Fournie T, Switzer C. Applied smouldering combustion for supporting a circular economy. In: Tudor T, editor. Resources management: global perspectives and initiatives. Royal Society of Chemistry; 2025. p. 176–219.

[9] Duchesne AL, Brown JK, Patch DJ, Major D, Weber KP, Gerhard JI. Remediation of PFAS-contaminated soil and granular activated carbon by smoldering combustion. Environ Sci Technol 2020;54(19):12631–40. https://doi.org/10.1021/acs.est.0c03058.

[10] Harrison BG, Major DW, Kinsman LL, Brown JK, Gabayet JLD, Gerhard JI, Patch DJ, Weber KP, Chernysheva L, Brown GM, Doudrick K, Abarca-Perez A, Peaslee GF, Pennell KD, Manz KE. Smoldering treatment of PFAS: investigation of mass balance and volumetric scale up for field implementation. ACS Omega 2025;10(28):30489–500. https://doi.org/10.1021/acsomega.5c02257.

[11] Solinger R, Grant GP, Scholes GC, Murray C, Gerhard JI. STARx Hottpad for smoldering treatment of waste oil sludge: proof of concept and sensitivity to key design parameters. Waste Manag Res 2020;38(5):554–66. https://doi.org/10.1177/0734242X20904430.

[12] Switzer C, Pironi P, Gerhard JI, Rein G, Torero JL. Volumetric scale-up of smouldering remediation of contaminated materials. J Hazard Mater 2014;268:51–60. https://doi.org/10.1016/j.jhazmat.2013.11.053.

[13] Murray C. Field trials of ex situ smouldering treatment (STARx) of oil sludge [MESc]. London, Canada: The University of Western Ontario; 2019.

[14] Jouhara H, Khordehgah N, Almahmoud S, Delpech B, Chauhan A, Tassou SA. Waste heat recovery technologies and applications. Therm Sci Eng Prog 2018;6:268–89. https://doi.org/10.1016/j.tsep.2018.04.017.

[15] Morales RB, DeGroot CT, Scholes GC, Gerhard JI. Understanding, controlling and optimising the cooling of waste thermal treatment beds including STARx Hottpads. Waste Manag Res 2022:0734242X221076308. https://doi.org/10.1177/0734242X221076308.

[16] Sabadell G, Thomas D, Bireta P, Scholes G, Murray C, Boulay B, Grant G, Major D. Treatment of oil-impacted soil and oily waste: overview of two field demonstration projects. In: SPE international conference and exhibition on health, safety, security, environment, and social responsibility. Abu Dhabi, UAE: Society of Petroleum Engineers; 2018. SPE-190566-MS.

[17] Shi B, Su H, Li J, Qi H, Zhou F, Torero JL, Chen Z. Clean power generation from the intractable natural coalfield fires: turn harm into benefit. Sci Rep 2017;7(1):5302. https://doi.org/10.1038/s41598-017-05622-4.

[18] Duque JVF, Bittencourt FLF, Martins MF, Debenest G. Developing a combustion-driven reactor for waste conversion. Energy 2021:121489. https://doi.org/10.1016/j.energy.2021.121489.

[19] Duque JVF, Martins MF, Bittencourt FLF, Debenest G. Relevant aspects of propagating a combustion front in an annular reactor for out-of-bed heat recovery. Exp Therm Fluid Sci 2022;133:110575. https://doi.org/10.1016/j.expthermflusci.2021.110575.

[20] Bittencourt FLF, Martins MF, Orlando MTD, Galvão ES. The proof-of-concept of a novel feces destroyer latrine. J Environ Chem Eng 2022;10(1):106827. https://doi.org/10.1016/j.jece.2021.106827.

[21] Pan R, Lougou BG, Shuai Y, Debenest G. A multidimensional numeric study on smoldering-driven pyrolysis of waste polypropylene. Process Saf Environ Prot 2023. https://doi.org/10.1016/j.psep.2023.02.018.

[22] Pan R, Debenest G, Zanoni MAB. Numerical study of plastic waste pyrolysis driven by char smoldering. Process Saf Environ Prot 2022;165:46–56. https://doi.org/10.1016/j.psep.2022.06.060.

[23] Pan R, Debenest G. Numerical investigation of a novel smoldering-driven reactor for plastic waste pyrolysis. Energy Convers Manag 2022;257:115439. https://doi.org/10.1016/j.enconman.2022.115439.

[24] Bittencourt FLF, Martins MF, Orlando MTD. Integrating in-bed gas looping and CO2 capture in the FeD-Latrine. Sci Total Environ 2023;859:160133. https://doi.org/10.1016/j.scitotenv.2022.160133.

[25] Fabris I, Cormier D, Gerhard JI, Bartczak T, Kortschot M, Torero JL, Cheng Y-L. Continuous, self-sustaining smouldering destruction of simulated faeces. Fuel 2017;190:58–66. https://doi.org/10.1016/j.fuel.2016.11.014.

[26] Rashwan TL, Torero JL, Gerhard JI. Heat losses in applied smouldering systems: sensitivity analysis via analytical modelling. Int J Heat Mass Tran 2021;172:121150. https://doi.org/10.1016/j.ijheatmasstransfer.2021.121150.

[27] Yermán L, Hadden RM, Carrascal J, Fabris I, Cormier D, Torero JL, Gerhard JI, Krajcovic M, Pironi P, Cheng Y-L. Smouldering combustion as a treatment technology for faeces: exploring the parameter space. Fuel 2015;147:108–16. https://doi.org/10.1016/j.fuel.2015.01.055.

[28] Rashwan TL, Torero JL, Gerhard JI. The improved energy efficiency of applied smouldering systems with increasing scale. Int J Heat Mass Tran 2021;177:121548. https://doi.org/10.1016/j.ijheatmasstransfer.2021.121548.

[29] Morales RB. Engineering cooling time and waste heat recovery for thermal treatment beds. Canada: The University of Western Ontario; 2022.

[30] Rashwan TL, Torero JL, Gerhard JI. Heat losses in a smouldering system: the key role of non-uniform air flux. Combust Flame 2021;227:309–21. https://doi.org/10.1016/j.combustflame.2020.12.050.

[31] Zanoni MAB, Wang J, Gerhard JI. Understanding pressure changes in smouldering thermal porous media reactors. Chem Eng J 2021;412:128642. https://doi.org/10.1016/j.cej.2021.128642.

[32] Zanoni MAB, Torero JL, Gerhard JI. Determination of the interfacial heat transfer coefficient between forced air and sand at Reynold's numbers relevant to smouldering combustion. Int J Heat Mass Tran 2017;114(Supplement C):90–104. https://doi.org/10.1016/j.ijheatmasstransfer.2017.06.020.

[33] Zanoni MAB, Torero JL, Gerhard JI. The role of local thermal non-equilibrium in modelling smouldering combustion of organic liquids. Proc Combust Inst 2019;37(3):3109–17. https://doi.org/10.1016/j.proci.2018.05.177.

[34] Sabadell G, Scholes G, Thomas D, Murray C, Bireta P, Grant G, Major D. Ex situ treatment of organic wastes or oil-impacted soil using a smoldering process. WIT Trans Ecol Environ 2019;231:367–76. https://doi.org/10.2495/WM180341.

[35] Thomas D, Bireta P, McVey K, Segal D, Hudson M, Sami B-H, Gabriel S. A novel, cost effective and easily scaled solution for on-site treatment of oily wastes. International petroleum technology conference. Dhahran, kingdom of Saudi arabia. International Petroleum Technology Conference; 2020. IPTC-19951-MS.

[36] Rashwan TL, Fournie T, Torero JL, Grant GP, Gerhard JI. Scaling up self-sustained smouldering of sewage sludge for waste-to-energy. Waste Manage (Tucson, Ariz) 2021;135:298–308. https://doi.org/10.1016/j.wasman.2021.09.004.

[37] Ma L, Qiao Y, Huang J, Zhang M, Zhang J, Qin P, Sun Z. Self-sustained smouldering treatment technology for high-moisture sludge: pilot-scaled tests with continuous operation. Waste Manage (Tucson, Ariz) 2024;188:86–94. https://doi.org/10.1016/j.wasman.2024.08.006.

[38] Ma L, Yan C, Feng C, Qiao Y, Huang J, Fang Q, Zhang C. Experimental investigation on self-sustained smouldering of food-processing sludge with extremely high moisture content: from laboratory-scale to pilot-scale volumetric scale-up. Waste Manage (Tucson, Ariz) 2023;158:13–22. https://doi.org/10.1016/j.wasman.2023.01.005.

[39] Wang J, Grant GP, Gerhard JI. The influence of porous media heterogeneity on smouldering remediation. J Contam Hydrol 2021;237:103756. https://doi.org/10.1016/j.jconhyd.2020.103756.

[40] Miry SZ, Zanoni MAB, Rashwan TL, Torero JL, Gerhard JI. Investigation of multi-dimensional transfer effects in applied smouldering systems: a 2D numerical modelling approach. Combust Flame 2022;246:112385. https://doi.org/10.1016/j.combustflame.2022.112385.

[41] Rashwan TL, Zanoni MAB, Wang J, Torero JL, Gerhard JI. Elucidating the characteristic energy balance evolution in applied smouldering systems. Energy 2023;273:127245. https://doi.org/10.1016/j.energy.2023.127245.

[42] Anderson R, Shiri S, Bindra H, Morris JF. Experimental results and modeling of energy storage and recovery in a packed bed of alumina particles. Appl Energy 2014;119:521–9. https://doi.org/10.1016/j.apenergy.2014.01.030.

[43] Kuznetsov AV. An investigation of a wave of temperature difference between solid and fluid phases in a porous packed bed. Int J Heat Mass Tran 1994;37(18):3030–3. https://doi.org/10.1016/0017-9310(94)90358-1.

[44] Martins MF, Salvador S, Thovert JF, Debenest G. Co-current combustion of oil shale – Part 2: structure of the combustion front. Fuel 2010;89(1):133–43. https://doi.org/10.1016/j.fuel.2009.06.040.

[45] Klippel MS, Xavier AV, Bittencourt FLF, Rashwan TL, Martins MF. On the design of smoldering reactors for out-of-bed heat recovery. Chem Eng Res Des 2025;220:438–49. https://doi.org/10.1016/j.cherd.2025.06.024.